GHGT-12

# Coupled modeling of multiphase flow and fault poromechanics during geologic $CO_2$ storage

Birendra Jha\*, Ruben Juanes

*Massachusetts Institute of Technology, 77 Massachusetts Avenue, Cambridge, MA 02139, USA*

## Abstract

Coupling between fluid flow and mechanical deformation in porous media plays a critical role in geologic storage of $CO_2$. One of the key issues in simulation of $CO_2$ sequestration is the ability to describe the mechanical and hydraulic behavior of faults, and the influence of the stress tensor and change in pressure on fault slip. Here, we present a new computational approach to model coupled multiphase flow and geomechanics of faulted reservoirs. We represent faults as surfaces embedded in a three-dimensional medium by using zero-thickness interface elements to accurately model fault slip under dynamically evolving fluid pressure and fault strength. We incorporate the effect of fluid pressures from multiphase flow in the mechanical stability of faults by defining a fault pressure. We employ a rigorous formulation of nonlinear multiphase geomechanics based on the increment in mass of fluid phases, instead of the change in porosity. Our nonlinear formulation is required to properly model systems with high compressibility or strong capillarity, as can be the case for geologic $CO_2$ sequestration. To account for the effect of surface stresses along fluid-fluid interfaces, we use the equivalent pore pressure in the definition of multiphase effective stress. We develop a numerical simulation tool by coupling a multiphase flow simulator with a mechanics simulator, using the unconditionally stable fixed-stress scheme for a computationally efficient sequential solution of two-way coupling between flow and geomechanics. We validate our modeling approach using several synthetic test cases that illustrate the onset and evolution of earthquakes from fluid injection.

* Corresponding author. Tel.: +1-617-253-7191; fax: +1-617-253-7475.
*E-mail address:* bjha@mit.edu

## 1. Introduction

Injection of $CO_2$ requires displacement and compression of the ambient groundwater, and an overpressurization of the target aquifer, which could fracture the caprock [16], trigger seismicity and cause shear slip on pre-existing faults [125,126,127,30,24,25,103,104], and potentially compromise the caprock by activating faults [162]. Overpressurization can limit the $CO_2$ storage capacity of the aquifer [145]. Despite the growing environmental, industrial, and economic importance of coupled flow and geomechanics, many aspects remain poorly understood. One of the fundamental unresolved issues is the ability to describe the mechanical and hydraulic behavior of faults, and the influence of the full stress tensor and change in pressure on fault slip. Injection and production of fluids from a geologic reservoir induce changes in the state of stress, both within and outside the reservoir, and these can affect the stability of preexisting faults. The effects of injection and production depend on the initial state of stress, the elastic moduli of the geologic structures, and the fault frictional properties. The effects are not always intuitively obvious and should be quantified using geomechanical models. This requires the development of a new generation of geomechanical models that include coupling between fluid flow and fault motion.

Currently, geomechanical models typically treat faults as failure zones that are discretized as three-dimensional elements where the rheology is allowed to be different (e.g., plastic with weakening failure) than in the rest of the domain (e.g., elastoplastic with hardening law) [126,24,25]. This approach has several limitations, including the inability to model actual slip along a surface of discontinuity, and the dependence of the simulation results on the level of grid refinement. Other models represent faults as surfaces using interface elements [47], but so far these models are uncoupled to flow, and they model fault slip using a penalty method [58]. Such methods require a priori selection of the penalty parameters for the fault, and therefore cannot represent dynamically evolving fault strength, such as slip-weakening or rate- and state-friction models [40].

The interactions between flow and geomechanics have been modeled computationally using various coupling schemes [39,74,75,97,101,136,137,148,149,150,82,83,84,85]. In the fully implicit method, one solves the coupled discrete nonlinear system of equations simultaneously, typically using the Newton-Raphson scheme [144,114,92,93,47]. The fully implicit method guarantees unconditional stability if the mathematical problem is well posed, but the simulation of flow and geomechanics for realistic fields becomes computationally very expensive [136,148,75]. Sequential approaches to modeling coupled flow and geomechanics are highly desirable because they offer the flexibility of using separate simulators for each subproblem [45,129,101,124]. The design and analysis of sequential methods with appropriate stability properties for poromechanics and thermomechanics has a long history [159,7,8,6,136,97,74]. Recently, a new sequential method for coupled flow and geomechanics, termed the ''fixed-stress split,'' has been proposed and analyzed [83,84,85]. Stability and convergence analyses have shown that the fixed-stress split inherits the dissipation properties of the continuum problem and is therefore unconditionally stable, both in the linear (poroelastic) and nonlinear (poroelastoplastic) regime. The analysis has shown that the fixed-stress split enjoys excellent convergence properties, even in the quasi-incompressible limit. It has also been shown recently that the stability and convergence properties of the fixed-stress split for single-phase flow carry over to multiphase systems if a proper definition of pore pressure, the ''equivalent pore pressure'' [32], is used [85].

In this article, we present a new computational model for coupled flow and geomechanics of faulted reservoirs. We couple a flow simulator with a mechanics simulator using the fixed-stress scheme [83]. We employ a rigorous formulation of nonlinear multiphase geomechanics [31] based on the increment in mass of fluid phases, instead of the more common, but less accurate, scheme based on the change in porosity [136,101,148,149,150,124]. Our nonlinear formulation is required to properly model systems with high compressibility or strong capillarity [31], as can be the case for geologic $CO_2$ sequestration [125,126], groundwater extraction from unconfined aquifers [52,59], and shale gas production [43]. To account for the effect of surface stresses along fluid-fluid interfaces, we use the equivalent pore pressure in the definition of multiphase effective stress [32,85]. We model faults as surfaces of discontinuity using interface elements [1]. This allows us to model stick-slip behavior on the fault surface for dynamically evolving fault strength.

## 2. Governing Equations

### 2.1. Balance Laws

We use a classical continuum representation in which the fluids and the solid skeleton are viewed as overlapping continua [11,33]. The governing equations for coupled flow and geomechanics are obtained from conservation of mass and balance of linear momentum. We assume that the deformations are small, that the geomaterial is isotropic, and that the conditions are isothermal. Let $\Omega$ be our domain of interest and $\partial\Omega$ be its closed boundary. Under the quasistatic assumption for earth displacements, the governing equation for linear momentum balance of the solid/fluid system can be expressed as

$$\nabla \cdot \boldsymbol{\sigma} + \rho_b \boldsymbol{g} = \boldsymbol{0},$$

(1)

where $\boldsymbol{\sigma}$ is the Cauchy total stress tensor, $\boldsymbol{g}$ is the gravity vector, and $\rho_b = \phi \sum_\beta^{n_{\text{phase}}} \rho_\beta S_\beta + (1 - \phi)\rho_s$ is the bulk density, $\rho_\beta$ and $S_\beta$ are the density and saturation of fluid phase $\beta$, and $\rho_s$ is the density of the solid phase, $\phi$ is the true porosity, and $n_{\text{phase}}$ is the number of fluid phases. The true porosity is defined as the ratio of the pore volume to the bulk volume in the current (deformed) configuration. Assuming that the fluids are immiscible, the mass-conservation equation for each phase $\alpha$ is

$$\frac{dm_\alpha}{dt} + \nabla \cdot \boldsymbol{w}_\alpha = \rho_\alpha f_\alpha,$$

(2)

where the accumulation term $dm_\alpha/dt$ describes the time variation of fluid mass relative to the motion of the solid skeleton, $\boldsymbol{w}_\alpha$ is the mass-flux of fluid phase $\alpha$ relative to the solid skeleton, and $f_\alpha$ is the volumetric source term for phase $\alpha$. The two balance equations (1) and (2) are coupled by virtue of poromechanics. On one hand, changes in the pore fluid pressure lead to changes in effective stress, and induce deformation of the porous material—such as ground subsidence caused by groundwater withdrawal. On the other hand, deformation of the porous medium affects fluid mass content and fluid pressure. The simplest model of this two-way coupling is Biot's macroscopic theory of poroelasticity [15,55,31]. In the remainder of this section we provide the mathematical description of poroelasticity for multiphase fluid systems.

### 2.2. Multiphase poromechanics

In the multiphase or partially saturated fluid system, it is not possible to linearize the equations of poroelasticity around a reference state because [31]:
1. Gases are very compressible,
2. Capillary pressure effects are intrinsically nonlinear, and
3. Phase saturations vary between 0 and 1 and, therefore, a typical problem samples the entire range of nonlinearity.

Therefore, following [31], we use the incremental formulation of poromechanics for multiphase systems, which does not assume physical linearization of total stress from the initial state to the current (deformed) state. We make a modeling assumption that allows us to express the deformation of a multiphase porous material in terms of the increment in applied total stresses and internal fluid pressures. We adopt an effective stress formulation in the multiphase poromechanics [17,18] because constitutive modeling of porous materials is usually done in terms of the effective stress. Under this formulation, we split the total stress on the porous material into two parts: one that is responsible for deformation of the solid skeleton (the effective stress), and another component that is responsible for changes in the fluid pressures,

$$\delta\boldsymbol{\sigma} = \boldsymbol{C}_{dr} : \delta\boldsymbol{\varepsilon} - \sum_\beta b_\beta \, p_\beta \boldsymbol{1},$$

(3)

where $b_\beta$ are the Biot coefficients for individual phases such that $\sum_\beta b_\beta = b$, where $b$ is the Biot coefficient of the saturated porous material. It is common to further assume that $b_\beta$ are proportional to the respective saturations $S_\beta$ [91,34,90].

The effective stress concept allows us to treat a multiphase porous medium as a mechanically equivalent single-phase continuum [81,108]. The appropriate form of the effective stress equation in a multiphase system is still an active area of research [61,32,108,153,107,85]. Here we use the concept of equivalent pressure [32] in the effective stress equation (Eq. (3)),

$$p_E = \sum_\beta S_\beta p_\beta - U,$$

(4)

where $U = \sum_\beta \int p_\beta dS_\beta$ is the interfacial energy computed from the capillary pressure relations [85]. The equivalent pressure accounts for the interface energy in the free energy of the system, and leads to a thermodynamically consistent and mathematically well-posed description of the multiphase fluid response to the solid deformation [85]. For a system with two phases, the wetting phase $w$ and the non-wetting phase $o$, the capillary pressure is

$$P_c(S_w) \equiv P_{wo}(S_w) = p_o - p_w,$$

(5)

and the interfacial energy is $U = \int_{S_w}^1 P_{wg} dS$. Assuming $b_\beta = bS_\beta$ [91,34,90], and using Eq. (4) in Eq. (3), we obtain the stress-strain relation- ship for multiphase linear poroelasticity:

$$\delta\boldsymbol{\sigma} = \delta\boldsymbol{\sigma}' - b\delta p_E \mathbf{1}, \qquad \delta\boldsymbol{\sigma}' = \boldsymbol{C}_{dr} : \delta\boldsymbol{\varepsilon}.$$

(6)

Once we have a definition of the effective stress in multiphase systems, we now express the change in the fluid mass in terms of the mechanical deformation and the change in the fluid pressures. In the deformed configuration, the mass of phase $\alpha$ per unit volume of porous medium is

$$m_\alpha = \rho_\alpha S_\alpha \phi (1 + \varepsilon_v),$$

(7)

Note that, by definition, the sum of all fluid phase saturations adds up to 1. For multiphase systems [31,32], we have

$$\left(\frac{dm}{\rho}\right)_\alpha = b_\alpha d\varepsilon_v + \sum N_{\alpha\beta} dp_\beta,$$

(8)

where $\boldsymbol{N} = \boldsymbol{M}^{-1}$ is the inverse Biot modulus. In a multiphase system, the Biot modulus is a symmetric positive definite tensor $\boldsymbol{M} = [M_{\alpha\beta}]$, and the Biot coefficient is a vector. To determine the coupling coefficients $N_{\alpha\beta}$ as a function of the primary variables (pressure, saturations, and displacements) and rock and fluid properties we develop an alternate expression for the differential increment in fluid mass. Using Eq. (7),

$$dm_\alpha = d(\rho_\alpha S_\alpha \phi(1 + \varepsilon_v)),$$

(9)

which can be expanded as

$$\left(\frac{dm}{\rho}\right)_\alpha = \phi \frac{\partial S_\alpha}{\partial P_{\alpha\beta}} dP_{\alpha\beta} + \phi S_\alpha c_\alpha dp_\alpha + \phi S_\alpha d\varepsilon_v + S_\alpha d\phi,$$

(10)

where $c_\alpha$ is the compressibility of the fluid phase $\alpha$, and $\partial S_\alpha / \partial P_{\alpha\beta}$ is the inverse capillary pressure derivative. Above, repeated indices do not imply summation and we have assumed infinitesimal deformations. We can express the increment in porosity $d\phi$ as a function of the volumetric effective stress $d\sigma'_v$ to obtain a closed-form expression

of Eq. (10). Let $V_s = V_b - V_p$ be the volume of the solid matrix, and $d\varepsilon_{sv} = dV_s/V_s = d\sigma_{sv}/K_s$ be the volumetric dilation of the solid matrix, where $\sigma_{sv}$ is the volumetric matrix stress. From an expansion of $d\phi$ we can write the incremental form of strain partition as

$$(1 - \phi)d\varepsilon_v = (1 - \phi)d\varepsilon_{sv} + d\phi.$$
(11)

Similarly, the volumetric Cauchy total stress can be partitioned into the volumetric matrix stress and the fluid pressure as

$$d\sigma_v = (1 - \phi)d\sigma_{sv} - \phi dp_E.$$
(12)

Substituting $d\sigma_{sv}$ from Eq. (12) into Eq. (11), we obtain

$$d\phi = \frac{b - \phi}{K_{dr}}(d\sigma'_v + (1 - b)dp_E).$$
(13)

Eq. (13) implies that an increment in porosity is related to increments in volumetric effective stress and fluid pressures. Substituting $d\varepsilon_v$ from Eq. (6) and $d\phi$ from Eq. (13) into Eq. (10) allows us to express the increment in the phase mass as a function of the increments in the total volumetric stress and phase pressures. Equating this to Eq. (8) yields the desired expressions for the coupling coefficients $N_{\alpha\beta}$.

Finally, we obtain the multiphase flow equation for phase $\alpha$ in a poroelastic medium by substituting the two constitutive relations, the effective stress equation, Eq. (6), and the fluid mass increment equation, Eq. (8), in the mass balance equation, Eq. (2):

$$\frac{\partial}{\partial t}\left(\rho_\alpha \sum_\beta \left(N_{\alpha\beta} + \frac{b_\alpha b_\beta}{K_{dr}}\right)p_\beta\right) + \frac{1}{K_{dr}}\frac{\partial}{\partial t}(\rho_\alpha b_\alpha \sigma_v) + \nabla \cdot \boldsymbol{w}_\alpha = \rho_\alpha f_\alpha, \qquad \forall \alpha = 1, \dots, n_{\text{phase}}$$
(14)

The role of $\boldsymbol{N}$ and $\boldsymbol{b}$ as the coupling coefficients among different fluid phases and the solid phase is evident from the above equation. The bulk density, $\rho_b$, in the mechanical equilibrium equation, Eq. (1), also acts as a coupling parameter because it is a function of the porosity and the phase saturations. Because we assume that the fluids are immiscible, the mass-flux of phase $\alpha$ is $\boldsymbol{w}_\alpha = \rho_\alpha \boldsymbol{v}_\alpha$, where we adopt the traditional multiphase-flow extension of Darcy's law [106,11]:

$$\boldsymbol{v}_\alpha = \frac{\boldsymbol{k}k_\alpha^r}{\mu_\alpha}(\nabla p_\alpha - \rho_\alpha \boldsymbol{g}),$$
(15)

where $\mu_\alpha$ and $k_\alpha^r$ are the dynamic viscosity and the relative permeability of phase $\alpha$ in presence of other fluid phases.

## 3. Poromechanics of Faults

There are two basic approaches to represent faults in a three-dimensional medium: either as a three-dimensional fault zone (e.g., [126]) or a two-dimensional fault surface (e.g., [77,102,46]). The advantage of representing faults as surfaces of discontinuity is that they can more faithfully describe the localized (discontinuous) displacement at the fault, and that one can incorporate models of dynamic frictional strength (like the rate- and state-friction model [40]) capable of reproducing runaway fault slip characteristic of earthquakes. Moreover, introducing discrete fault surfaces does not preclude modeling an adjacent fault zone with appropriate rheology.

A central feature of our work is that we treat faults as surfaces of discontinuity embedded in the continuum, across which displacement is allowed to be discontinuous to recognize the possibility of fault slip (Fig. 1). We use zero-thickness elements, also known as interface elements or cohesive elements in the finite element literature

[60,14,27,57,88], to represent the fault surfaces. Mathematically, the fault surface is treated as an interior boundary between the two adjacent domains. The two sides of the fault surface, which need not be planar, are designated as the '+' side and the '−' side, and the fault normal vector, $\boldsymbol{n}$, points from the negative side to the positive side. Slip on the fault is the displacement of the positive side relative to the negative side,

$$(\boldsymbol{u}_+ - \boldsymbol{u}_-) - \boldsymbol{d} = \boldsymbol{0} \quad \text{on} \quad \Gamma_f,$$

(16)

where $\boldsymbol{u}_+$ and $\boldsymbol{u}_-$ are the displacements on the two sides of the fault surface, denoted by $\Gamma_f$, and $\boldsymbol{d}$ is the fault slip vector. Fault slip is governed by the effective traction on the fault, which is a function of the effective stress tensors on both sides of the fault, the fault normal direction, and the fault constitutive law. We impose the effective traction on the fault by introducing a Lagrange multiplier, $\boldsymbol{l}$, which is a force per unit area required to satisfy the equilibrium equation for a given relative displacement, $\boldsymbol{d}$, across the fault. The magnitude of the effective normal traction on the fault is

$$\sigma'_n = \boldsymbol{l} \cdot \boldsymbol{n}.$$

(17)

A positive value of $\sigma'_n$ indicates that a tensile effective stress is transmitted across the fault surface. The Kuhn-Tucker conditions of contact mechanics are obeyed such that no penetration occurs and the effective normal traction stays compressive at the contact surface. The shear traction vector is, by definition, tangent to the fault surface and its magnitude is

$$\tau = |\boldsymbol{l} - \sigma'_n \boldsymbol{n}|.$$

(18)

We use the Mohr-Coulomb theory to define the stability criterion for the fault [73]. When the shear traction on the fault is below the friction stress, $\tau \leq \tau_f$, the fault does not slip. When the shear traction is larger than the friction stress, $\tau > \tau_f$, the contact problem is solved to determine the Lagrange multipliers and slip on the fault, such that the Lagrange multipliers are compatible with the frictional stress.
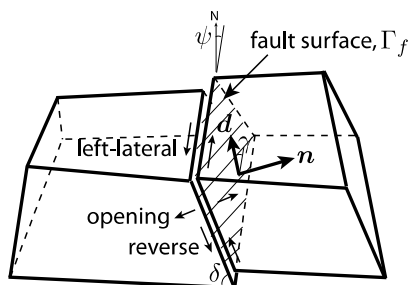


Fig. 1: Schematic of a 2D fault surface in a 3D domain. Discontinuity in the displacement across the fault is illustrated through the slip vector, $\boldsymbol{d}$, on the fault. Here, slip is assumed to be in the fault plane with no opening. The fault normal or $\boldsymbol{n}$, strike angle $\psi$, dip angle $\delta$, and slip rake angle $\gamma$ are defined in the global coordinate system. The fault coordinate system is defined in terms of tangential and normal motion on the fault with positive values associated with left-lateral, reverse, and opening motions.

### 3.1. Fault Pressure in the Failure Criterion

Traditionally, in the Andersonian faulting theory [5], fault slip is modeled in a "dry environment," that is, in the absence of fluids. While, in some cases, the presence of fluid has been recognized through the effective stress concept, the dynamics of flow was not included for reasons of conceptual and computational simplicity, as well as for the belief that fluid flow played a secondary role in the release of tectonic stresses [69,119]. The effect of pore pressure was accounted for by modifying the coefficient of fault friction $\mu_f$ [66,67], an approach later suggested to be "unwise" [13]. In the case of mature faults, the fault core permeability can be low due to comminution of grains while the damaged host rock permeability can be high due to fractures [138,140,29,22]. In addition, the permeability

can vary substantially across the fault during the seismic cycle [139,141]. As a result, pore pressures can be significantly different across the fault [142,120,29].

A difference in fluid pressure across the fault leads to a pressure jump $[\![p]\!]_{\Gamma_f} = p_+ - p_-$, where $p_+$ and $p_-$ are the equivalent multiphase pressures (Eq. (4)) on the "positive" and the "negative" side of the fault. One of the key features of the 2-D representation of faults is the ability to reproduce a finite jump in the pressure, $[\![p]\!]_{\Gamma_f}$, across the fault. This pressure jump leads to a discontinuity in the effective stress across the fault, such that the total stress is continuous

$$\boldsymbol{\sigma'}_- \cdot \boldsymbol{n} - b p_- \boldsymbol{n} = \boldsymbol{\sigma'}_+ \cdot \boldsymbol{n} - b p_+ \boldsymbol{n},$$

(19)

a requirement for momentum balance on the fault. This gives rise to the question of how to incorporate in the formulation the pressure jump across a fault. This is important because it determines the stability of the fault.

Fault stability can be assessed by evaluating the stability criterion on both sides of the fault separately. The side of the fault where the criterion is met first determines the fault stability. Equivalently, this can be achieved by defining a *fault pressure* that is a function of the pressures on the two sides, $p_+$ and $p_-$. Introducing the fault pressure allows us to uniquely define the *effective* normal traction on the fault, $\sigma'_n$, and determine the fault friction $\tau_f$. Since the stability criterion, $\tau \le \tau_f$, is first violated with the larger pressure, we define the fault pressure, $p_f$, as

$$p_f = \max(p_+, p_-).$$

(20)

Our definition of fault pressure is a natural result of our fault representation, rather than a conservative assumption. Note that estimating the fault pressure as the arithmetic average of the pressures on the two sides, as proposed in the case of tensile fractures [133,134,135], may incorrectly delay the onset of shear failure. By univocally defining the pressure at the fault (Eq. (20)), we also univocally define the effective traction at the fault (the Lagrange multiplier *l*), something that is required to evaluate the fault stability criterion.

## 4. Implementation into a Simulation Software

We developed a coupled multiphase flow and geomechanical simulator by coupling the General Purpose Research Simulator (GPRS) [23,113] as the flow simulator, and PyLith [1,2] as the mechanics simulator. Below we describe the major steps in the development of this coupled simulator.

### 4.1. The flow simulator

GPRS is a general purpose, object-oriented, reservoir simulator for multiphase/multicomponent subsurface flows. It treats element connections through a general connection list, which allows for both structured and unstructured grids. GPRS is capable of handling complex production and injection scenarios in the field, such as wells perforated at multiple depths and flowing under variable rate and pressure controls. The original simulator [23,113] does not account for coupling with the mechanical deformation, and it models the mechanical behavior of the system through a user-provided rock compressibility [9]. We modified and extended the original code to implement the coupling with the mechanics simulator. In particular, we implemented the functionality to compute the modified accumulation term in the fluid phase mass balance equations. We also modified the setup of the linear system to implement the flow step of the fixed-stress sequential solution scheme [83].

### 4.2. The geomechanics simulator

PyLith is a finite element code for the simulation of static and dynamic large-scale deformation problems [1,2]. Much of its development has been motivated by the modeling of earthquake physics; however, its applicability extends to problems at any other scale, such as the reservoir scale or the laboratory scale. Some of the advantages of PyLith are (1) it is an open-source code and can be modified for specific purposes; (2) it is written using C++ and Python languages and is extendable; (3) it is suitable for parallel computing; (4) it allows localized deformation

along discrete features, such as faults; and (5) it is well integrated with meshing codes, such as LaGriT for tetrahedral meshes [87] and CUBIT for both tetrahedral and hexahedral meshes [36]. PyLith uses an implicit formulation to solve quasi-static problems and an explicit formulation to solve dynamic rupture problems. Originally, PyLith is not coupled to any fluid flow model. We modified the code of PyLith version 1.8.0 and coupled it with the flow simulator, GPRS. In particular, we implemented a C++ class, iGPRS, to allow communication between the flow and the mechanics simulators. iGPRS provides the functionality required for exchanging information (pressures, saturations, and volumetric total stress) between the two simulators.

PyLith supports distributed memory parallelization (Message Passing Interface or MPI) whereas GPRS's parallelization is based on the shared memory architecture (Multiprocessing or OpenMP). We integrated the two such that we can run the coupled simulator on a cluster with multiple compute nodes (distributed memory) where individual nodes have multiple cores or processors (shared memory).

### 4.3. Grid

We use a single grid for both GPRS and PyLith. The grid is generated using CUBIT [36] or LaGriT [87] mesh generation software. We define geologic surfaces, material regions, faults, and pinch-outs during the geometry creation stage. Then we mesh the domain with hexahedral elements using a fine mesh in the reservoir domain and an increasingly coarse mesh in the overburden, underburden, and sideburden regions. We export the grid in a finite element format such as the Exodus-II format [36] for PyLith. We process the grid file using a MATLAB script to generate the equivalent finite volume grid in the domain with element centroid coordinates, element bulk volumes, and face transmissibilities in the Corner Point Geometry format [130]. Any grid elements lying outside the flow region of interest (e.g., in overburden and underburden) can be deactivated for the solution of the flow problem. GPRS uses the finite volume grid for simulating flow in the region of interest. The two simulators exchange pressures, saturations, and volumetric stress information inside this region.

### 4.4. Implementation of Faults

To support relative motion across fault surfaces, PyLith modifies the grid topology to create zero-thickness fault elements and adds additional degrees of freedom to hold the Lagrange multipliers and fault slip vectors at the Lagrange nodes [1,2] (Fig. 1 and 2). PyLith solves the contact problem iteratively in two steps. In the first step, the elasticity problem is solved over the entire domain to update the displacements and the fault tractions (Lagrange multipliers) corresponding to the current estimate of the slip. The Lagrange multipliers are compared with the friction stress on the fault and are adjusted to be compatible with the fault constitutive model. In the second step, the fault slip is updated corresponding to the adjustment in the Lagrange multipliers while assuming that the deformation due to slip is localized to the elements adjacent to the fault, that is, that displacements at non-fault nodes do not change from their values at the current Newton iteration. If the fault slips over the entire domain, such that the assumption of deformation being limited to the adjacent elements is not met, the convergence of the iterative scheme is poor. Also, if the fault friction coefficient changes significantly with slip (e.g., in rate- and state-dependent models), it leads to large changes in $\tau_f$ at every iteration and convergence may degrade. To improve convergence, a line-search routine is used as part of the iterative scheme to find the optimum perturbation in the Lagrange multipliers that minimizes the combined mismatch between the fault friction and the fault shear traction at all the fault nodes [2]. We modified PyLith's original line-search routine such that the inequality constraint, $\tau \leq \tau_f$, is always honored.
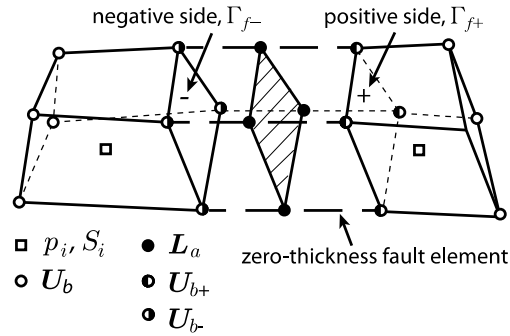
Fig. 2: Exploded view of our computational representation of a fault, illustrating different node types, locations of different variables, and the zero-thickness fault element. Fluid pressures $p_i$ and saturations $S_i$ are located at the element centers as they are discretized using the finite volume method. Displacements and Lagrange multipliers at the fault are discretized using the nodal-based finite element method. There are two types of nodes in the domain: the displacement nodes and the Lagrange nodes. The displacement nodes carry the displacements $U_{br}$ at the regular nodes, the displacements $U_{b+}$ on the positive side of the fault, and the displacements $U_{b-}$ on the negative side of the fault. The Lagrange nodes carry two types of fault variables: the Lagrange multipliers $L_b$ (related to fault tractions), and the fault slip $D_b$. The displacement nodes on the positive and negative sides, and the Lagrange nodes are collocated in the initial grid.

## 5. Representative Numerical Simulations

We illustrate the validity and applicability of our modeling approach through a number of representative simulations [76]. Some are verification problems and others are more realistic scenarios. We conduct these simulations using our coupled simulator. The 2-D numerical example simulations are conducted with a 2-D implementation in plane strain. Note that both GPRS and PyLith have been tested previously on respective benchmark problems, i.e., validation on flow-only problems for GPRS [23] and mechanics-only problems for PyLith [1]. Fault implementation in PyLith has been validated by comparison with analytical solutions from elastic dislocation theory [109].

### 5.1. Faulting due to $CO_2$ injection: Plane strain

This is an example of $CO_2$ injection in a deep confined aquifer for the purpose of geologic carbon sequestration [24]. The aquifer is hydraulically compartmentalized with a sealing fault that cuts across it. Storage capacity of the aquifer is limited by overpressurization and slip on the fault. As described in [24,76], we consider a two-dimensional plane-strain model with the fault under normal faulting conditions, that is, vertical principal stress due to gravity is the largest among the three principal stresses (Fig. 3). We choose a value of 0.7 for the ratio of horizontal to vertical initial total stress. After 20 days of injection, pressure in the aquifer increases approximately uniformly by 3.6 MPa (Fig. 4). Overpressure causes volumetric expansion of the aquifer (Fig. 5). This, in turn, results in an increase in the effective normal tractions throughout the aquifer, and an increase in the magnitude of shear tractions at the top and bottom boundaries of the aquifer.
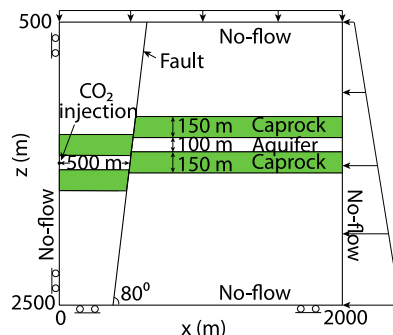


Fig. 3: Model of the CO2 injection plane strain case (adapted from [24]). The lateral compression is 0.7 times the overburden, and both increase with the lithostatic gradient. CO2 is injected in the confined aquifer at a depth of 1500 m. The aquifer is bounded on the top and bottom by a low-

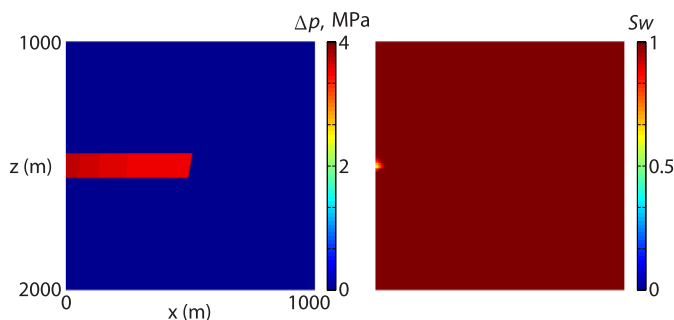permeability caprock, and the fault is impermeable to flow.



Fig. 4: CO$_2$ injection in the plane strain case. (left) Overpressure and (right) water saturation at $t = 21$ days.
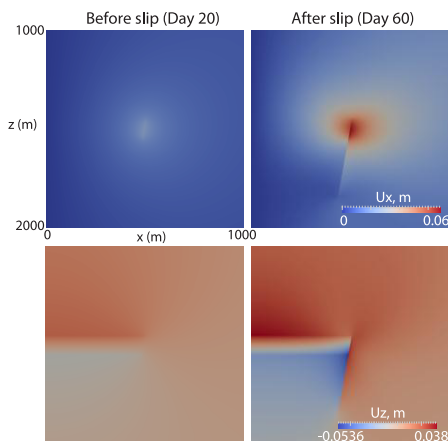


Fig. 5: CO$_2$ injection in the plane strain case. Displacement fields in the horizontal and vertical directions (top row and bottom row, respectively) at two different times: $t = 20$ days (left) and $t = 60$ days (right). Notice the discontinuity in the displacement field across the fault at $t = 60$ days as a result of slip. The rupture propagates along the fault, asymmetrically away from the nucleation point at 1550 m, with the longer part below the nucleation point due to the imposed normal faulting condition. After 60 days, the rupture span along the fault is approximately 400 m.

## 5.2. Faulting due to CO$_2$ injection: 3-D

This example is similar to the previous one, but here we consider a 4 x 4 x 2 km three-dimensional domain with a 200 m thick anticlinal aquifer (Fig. 6), and we use the rate and state-dependent friction model [40] for the fault friction. The rate and state constitutive parameters are $A = 0.002$, $B = 0.08$, the critical slip $d_c = 1$ cm, the static coefficient of friction $\mu_o = 0.4$, and the cohesive strength of fault $\tau_c = 0$. These values strongly favor unstable sliding on the fault. CO$_2$ is injected at a rate of 30 million standard cubic feet per day (17.64 kg/s) leading to overpressurization of the aquifer (Fig. 7). The anticline is off-centered in $y$, leading to asymmetry in the overpressure field. Rupture nucleates at the base of the aquifer after 202 days of injection and propagates on the fault along the bottom boundary of the aquifer (Fig. 8). After approximately two months, a second rupture sequence begins along the layer just above the base of the aquifer. At $t = 320$ days, the underburden rock layer below the aquifer reaches the failure criterion and slips, and the rupture subsequently propagates in both up-dip and down-dip directions on the fault with higher slip velocity in the down-dip direction. Downward slip is favored due to the imposed normal faulting condition.
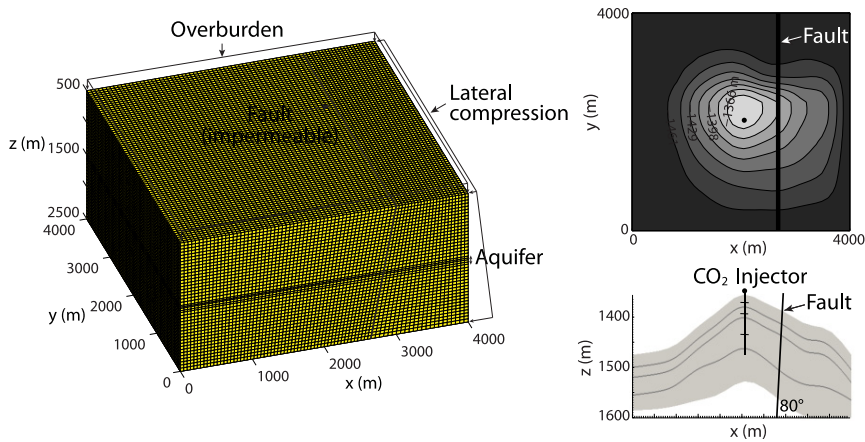
Fig. 6: CO₂ injection in a 3-D anticlinal aquifer. (left) The geomechanical domain, shown with the traction boundary conditions on the top and on the right boundaries. The lateral compression is 0.7 times the overburden, and both increase with the lithostatic gradient. Zero-normal displacement is imposed on all other boundaries. A no-flow boundary condition is imposed on all the boundaries. The flow domain is composed of the four layers marked as aquifer, and the injector is located near the center of the anticline. (top right) Plan view and (bottom right) cross-section view of the aquifer. Depth contours are marked in the plan view. The cross-section view is exaggerated in the vertical direction.
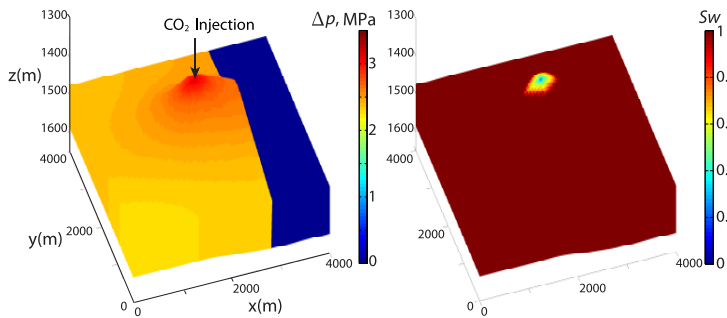


Fig. 7: CO₂ injection in a 3-D anticlinal aquifer. (left) Overpressure and (right) water saturation in the aquifer layers at $t = 202$ days, when fault slip starts.
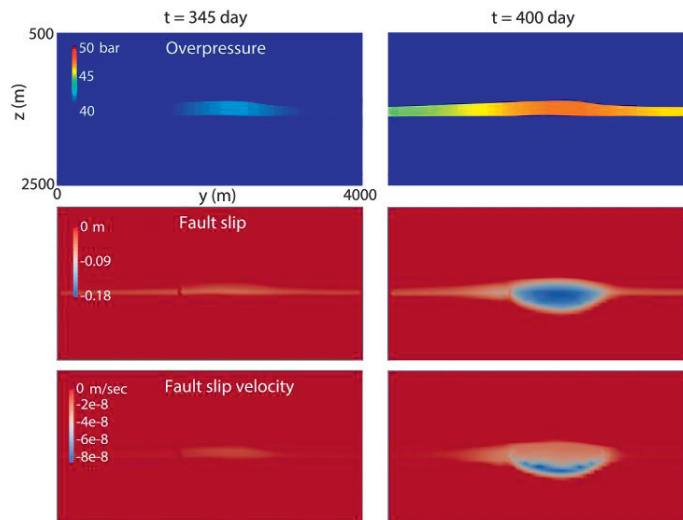
Fig. 8: $CO_2$ injection in a 3-D anticlinal aquifer. Evolution of pore pressure, fault slip, and fault slip velocity at two timesteps. The cross-section of the aquifer is visible in the top right plot. $CO_2$ injection in the aquifer leads to slip on the fault. The rupture initiates at the bottom of the aquifer and progresses both downdip and updip, with faster slip velocity downdip. The rupture front adopts an ellipsoidal shape following the profile of the aquifer, which is being pressurized. A video that shows the dynamics of fault rupture from the coupled flow-geomechanics simulation is included in the supporting information of [76].

## 6. Conclusions

We have presented a new computational model to simulate the coupling between multiphase flow and poromechanics of faults and developed a two-way coupled simulator that interlaces a geomechanics simulator (PyLith) with a multiphase flow simulator (GPRS). Our approach enjoys the following features:

1. It is computationally efficient because it relies on a sequential solution of the two-way coupled problem.

2. It is unconditionally stable, due to the use of the fixed-stress sequential split between multiphase flow and deformation. The model accounts rigorously for multiphase flow effects through a fully nonlinear poromechanics formulation.

3. It represents faults as surfaces embedded in a three-dimensional domain, therefore allowing for a discontinuous displacement field across the fault (fault slip). Our approach elucidates the role of the pressure discontinuity across the fault on the stability of the fault through the definition of a ''fault pressure.''

4. It incorporates realistic fault constitutive behavior, such as the rate- and state-dependent friction model, capable of simulating runaway fault slip typical of earthquakes.

We assume quasi-static mechanical deformation by neglecting the inertial term in the solid momentum balance equation, and we use an implicit time-marching scheme for the coupled simulation. While this is an excellent approximation prior to fault rupture, during fault slip the inertial term is not negligible due to propagation of seismic waves. We are currently extending the capabilities of our simulation tool to implement a dynamic implicit-explicit time-marching scheme that can take small time steps required to resolve the propagation of rupture on the fault, while taking orders of magnitude larger time steps during aseismic periods.

Our framework allows us to investigate fault slip and induced seismicity in underground reservoirs due to the coupled processes of fluid flow and mechanical deformation, such as those encountered during groundwater withdrawal and geologic $CO_2$ storage. In this work, we have demonstrated the effectiveness and applicability of our approach through a few synthetic, but realistic, examples. We are currently applying our computational model for the study of ground deformations detected from geodetic measurements via GPS and InSAR [64,44,146] and for the *post mortem* analysis of natural or induced earthquakes [59,151,80,20].

# References

[1] Aagaard B et al. PyLith User Manual, Version 1.8.0, Comput. Infrastruct. for Geodyn., Univ. of Calif., Davis, Calif.; 2012.

[2] Aagaard B et al. A domain decomposition approach to implementing fault slip in finite-element models of quasi-static and dynamic crustal deformation, J. Geophys. Res. Solid Earth 2013; 118, 3059–3079, doi:10.1002/jgrb.50217.

[3] Aavatsmark I. An introduction to multipoint flux approximations for quadrilateral grids, Comput. Geosci. 2002; 6, 405–432.

[4] Abousleiman Y et al. Mandel's problem revisited, Geotechnique 1996; 46, 187–195.

[5] Anderson EM. The Dynamics of Faulting and Dyke Formation With Application to Britain, Oliver and Boyd, New York; 1951.

[6] Armero F. Formulation and finite element implementation of a multiplicative model of coupled poro-plasticity at finite strains under fully saturated conditions, Comput. Methods Appl. Mech. Eng. 1999; 171, 205–241.

[7] Armero F, Simo JC. A new unconditionally stable fractional step method for non-linear coupled thermomechanical problems, Int. J. Numer. Methods Eng. 1992; 35, 737–766.

[8] Armero F, Simo JC. A priori stability estimates and unconditionally stable product formula algorithms for nonlinear coupled thermoplasticity, Int. J. Plasticity 1993; 9, 749–782.

[9] Aziz K, Settari A. Petroleum Reservoir Simulation, Elsevier, London, U. K.; 1979.

[10] Balay S et al. Efficient management of parallelism in object-oriented numerical software libraries, in Modern Software Tools in Scientific Computing, pp. 163–202, Birkhauser Press, Basel, Switzerland; 1997.

[11] Bear J. Dynamics of Fluids in Porous Media, John Wiley, New York, N. Y.; 1972.

[12] Bear J, Corapcioglu MY. Mathematical model for regional land subsidence due to water pumping, Water Resour. Res. 1981; 17, 937–958.

[13] Beeler NM et al. Pore fluid pressure, apparent friction, and Coulomb failure, J. Geophys. Res. 2000; 105, 25,533–25,542.

[14] Beer G. An isoparametric joint/interface element for finite element analysis, Int. J. Numer. Methods Eng. 1985; 21, 585–600.

[15] Biot MA. General theory of three-dimensional consolidation, J. Appl. Phys. 1941; 12, 155–164.

[16] Birkholzer JT, Zhou Q. Basin-scale hydrogeologic impacts of $CO_2$ storage: Capacity and regulatory implications, Int. J. Greenh. Gas Control 2009; 3, 745–756.

[17] Bishop AW. The principle of effective stress, Tekniske Ukeblad 1959; 39, 859–863.

[18] Bishop AW, Blight GE. Some aspects of effective stress in saturated and partly saturated soils, Geotechnique 1963; 13, 177–197.

[19] Brezis H. Functional Analysis, Sobolev Spaces and Partial Differential Equations, Springer, New York, N. Y.; 2011

[20] Brodsky EE, Lajoie LJ. Anthropogenic seismicity rates and operational parameters at the Salton Sea Geothermal Field, Science 2013; 341, 543–546.

[21] Brooks RH, Corey AT. Hydraulic properties of porous media, Hydrol. Pap. 3, pp. 892–898, Colo. State Univ., Fort Collins, Colo.; 1964

[22] Caine JS, Forster CB. Faults and Subsurface Fluid Flow in the Shallow Crust, Geophys. Monogr. Ser., vol. 113, edited by W. C. Haneberg et al., AGU, Washington, D. C.; 1999.

[23] Cao H. Development of techniques for general purpose simulators, PhD thesis, Stanford Univ., Stanford, Calif.; 2002.

[24] Cappa F, Rutqvist J. Impact of $CO_2$ geological sequestration on the nucleation of earthquakes, Geophys. Res. Lett. 2011; 38, L17313, doi:10.1029/2011GL048487.

[25] Cappa F, Rutqvist J. Modeling of coupled deformation and permeability evolution during fault reactivation induced by deep underground injection of $CO_2$, Int. J. Greenh. Gas Control 2011; 5, 336–346.

[26] Carder DS. Seismic investigations in the Boulder Dam area, 1940–1944, and the influence of reservoir loading on earthquake activity, Bull. Seismol. Soc. Am. 1945; 35, 175–192.

[27] Carol IA et al. A three dimensional elastoplastic joint element, in Fundamentals of Rock Joints, pp. 441–451, Centek, Lulea, Sweden; 1985.

[28] Carter RD, Tracy GW. An improved method for calculating water influx, Petrol. Trans., AIME 1960; 219, 415–417.

[29] Chester FM et al. Internal structure and weakening mechanisms of the San Andreas Fault, J. Geophys. Res. 1993; 98, 771–786.

[30] Chiaramonte L et al. Seal integrity and feasibility of CO2 sequestration in the Teapot Dome EOR pilot: Geomechanical site characterization, Environ. Geol. 2008; 54(8), 1667–1675.

[31] Coussy O. Mechanics of Porous Continua, John Wiley, Chichester, U. K.; 1995.

[32] Coussy O. Poromechanics, John Wiley, Chichester, U. K.; 2004.

[33] Coussy O. Poromechanics of freezing materials, J. Mech. Phys. Solids 2005; 53, 1689–1718.

[34] Coussy O et al. Constitutive modeling of unsaturated drying deformable materials, J. Eng. Mech. 1998; 124(6), 658–557.

[35] Coussy O et al. The equivalent pore pressure and the swelling and shrinkage of cement-based materials, Mater. Struct. 2004; 37, 15–20.

[36] CUBIT 13.2 User Documentation, Sandia Natl. Lab., Albuquerque, N. M.; 2013.

[37] Cueto-Felgueroso L, Juanes R. Forecasting long-term gas production from shale, Proc. Natl. Acad. Sci. U. S. A. 2013, 110, 19,660–19,661.

[38] Dake LP. Fundamentals of Reservoir Engineering, Elsevier, Oxford, U. K.; 1978.

[39] Dean RH et al. A comparison of techniques for coupling porous flow and geomechanics, Soc. Pet. Eng. J. 2006; 11, 132–140.

[40] Dieterich JH. Modeling of rock friction: 1. Experimental results and constitutive equations, J. Geophys. Res. 1979; 84, 2161–2168.

[41] Dieterich JH. Constitutive properties of faults with simulated gouge, in Mechanical Behaviour of Crustal Rocks: The Handin Volume, Geophys. Monogr. Ser., vol. 24, pp. 108–120, AGU, Washington, D. C.; 1981.

[42] Ellsworth WL. Injection-induced earthquakes, Science 2013; 341, 1–7.

[43] Engelder T. Capillary tension and imbibition sequester frack fluid in Marcellus gas shale, Proc. Natl. Acad. Sci. U. S. A. 2012; 109(52), E3625.

[44] Feigl KL et al. Space geodetic measurement of crustal deformation in central and southern California, 1984–1992, J. Geophys. Res. 1993;

98, 21,677–21,712.

[45] Felippa CA, Park KC. Staggered transient analysis procedures for coupled mechanical systems: Formulation, Comput. Methods Appl. Mech. Eng. 1980; 24, 61–111.

[46] Ferronato M et al. Numerical modeling of regional faults in land subsidence prediction above gas/oil reservoirs, Int. J. Numer. Anal. Methods Geomech. 2008; 32, 633–657.

[47] Ferronato M et al. A fully coupled 3-D mixed finite element model of Biot consolidation, J. Comput. Phys. 2010; 229(12), 4813–4830.

[48] Fetkovich MJ. A simplified approach to water influx calculations—Finite aquifer systems, J. Pet. Technol. 1971; 23, 814–828.

[49] Fialko Y, Simons M. Deformation and seismicity in the Coso geothermal area, Inyo County, California: Observations and modeling using satellite radar interferometry, J. Geophys. Res. 2000; 105, 21,781–21,793.

[50] Galloway DL, Burbey TJ. Review: Regional land subsidence accompanying groundwater extraction, Hydrogeol. J. 2011; 19, 1459–1486.

[51] Galloway DL et al. Detection of aquifer system compaction and land subsidence using interferometric synthetic aperture radar, Antelope Valley, Mojave Desert, California, Water Resour. Res. 1998; 34, 2573–2585.

[52] Gambolati G, Freeze R. Mathematical simulation of the subsidence of Venice: 1. Theory, Water Resour. Res. 1973; 9, 721–733.

[53] Gambolati G et al. The importance of poro-elastic coupling in dynamically active aquifers of the Po river basin, Italy, Water Resour. Res. 2000; 36, 2443–2459.

[54] Garcia JE. Fluid dynamics of carbon dioxide disposal into saline aquifers, PhD dissertation, Univ. of Calif., Berkeley, Calif.; 2003.

[55] Geertsma J. The effect of fluid pressure decline on volumetric change of porous rocks, Trans. AIME 1957; 210, 331–340.

[56] Geertsma J. A basic theory of subsidence due to reservoir compaction: The homogeneous case, Verhandelingen Kon. Ned. Geol. Mijnbouwk. Gen. 1973; 28, 43–62.

[57] Gens A et al. An interface element formulation for the analysis of soil-reinforcement interaction, Comput. Geotech. 1988; 7, 133–151.

[58] Glowinsky R, Le Tallec P. Augmented Lagrangian and Operator-Splitting Methods in Nonlinear Mechanics, Soc. Ind. Appl. Math. 1989; Philadelphia, PA.

[59] Gonzalez PJ et al. The 2011 Lorca earthquake slip distribution controlled by groundwater crustal unloading, Nat. Geosci. 2012; 5, 821–825.

[60] Goodman RE et al. A model for the mechanics of jointed rock, J. Soil Mech. 1968; 94, 637–659.

[61] Gray WG, Schrefler BA. Thermodynamic approach to effective stress in partially saturated porous media, Eur. J. Mech.-A/Solids 2001; 20, 521–538.

[62] Gunasekera D et al. A multi-point flux discretization scheme for general polyhedral grids, paper SPE 48855 presented at 6th SPE International Oil and Gas Conference and Exhibition 1998; Society of Petroleum Engineers, Beijing, China.

[63] Gupta HK. A review of recent studies of triggered earthquakes by artificial water reservoirs with special emphasis on earthquakes in Koyna, India, Earth Sci. Rev. 2002; 58, 279–310.

[64] Hager BH et al. Measurement of crustal deformation using the Global Positioning System, Annu. Rev. Earth Planet. Sci. 1991; 19, 351–382.

[65] Hanks TC, Kanamori H. A moment magnitude scale, J. Geophys. Res. 1979; 84, 2348–2350.

[66] Harris RA, Simpson RW. Changes in static stress on southern California faults after the 1992 Landers earthquake, Nature 1992; 360, 251–254.

[67] Harris RA et al. Influence of static stress changes on earthquake locations in southern California, Nature 1995; 375, 221–224.

[68] Howarth RW et al. Methane and the greenhouse-gas footprint of natural gas from shale formations, Clim. Change 2011; 106, 679–690.

[69] Hubbert MK, Rubey WW. Role of fluid pressure in mechanics of overthrust faulting. I. Mechanics of fluid-filled porous solids and its application to overthrust faulting, Geol. Soc. Am. 1959; 70, 115–166.

[70] Hughes TJR. The Finite Element Method: Linear Static and Dynamic Finite Element Analysis, Prentice Hall, Englewood Cliffs, N. J; 1987.

[71] IPCC (2005), Special Report on Carbon Dioxide Capture and Storage, edited by B. Metz et al., Cambridge Univ. Press, Cambridge, U. K.; 2005.

[72] Jackson RB et al. Increased stray gas abundance in a subset of drinking water wells near Marcellus shale gas extraction, Proc. Natl. Acad. Sci. U. S. A. 2013; 110(28), 11,250–11,255.

[73] Jaeger JC, Cook NGW. Fundamentals of Rock Mechanics, Chapman and Hall, London, U. K.; 1979.

[74] Jeannin L et al. Accelerating the convergence of coupled geomechanical–reservoir simulations, Int. J. Numer. Anal. Methods Geomech. 2007; 31, 1163–1181.

[75] Jha B, Juanes R. A locally conservative finite element framework for the simulation of coupled flow and reservoir geomechanics, Acta Geotech. 2007; 2, 139–153.

[76] Jha B, Juanes R. Coupled multiphase flow and poromechanics: a computational model of pore-pressure effects on fault slip and earthquake triggering. Water Resour. Res. 2014; 50, doi:10.1002/2013WR015175.

[77] Juanes R et al. A general and efficient formulation of fractures and boundary conditions in the finite element method, Int. J. Numer. Methods Eng. 2002; 54(12), 1751–1774.

[78] Juanes R et al. Impact of relative permeability hysteresis on geological $CO_2$ storage, Water Resour. Res. 2006; 42, W12418, doi:10.1029/2005WR004806.

[79] Juanes R et al. No geologic evidence that seismicity causes fault leakage that would render large-scale carbon capture and storage unsuccessful, Proc. Natl. Acad. Sci. U. S. A. 2012; 109(52), E3623.

[80] Keranen KM et al. Potentially induced earthquakes in Oklahoma, USA: Links between wastewater injection and the 2011 Mw 5.7 earthquake sequence, Geology 2013; 41, 699–702.

[81] Khalili N et al. Effective stress in unsaturated soils: A review with new evidence, Int. J. Geomech. 2004;, 4, 115–126.

[82] Kim J  et al. Stability and convergence of sequential methods for coupled flow and geomechanics: Drained and undrained splits, Comput. Methods Appl. Mech. Eng. 2011; 200, 2094–2116.

[83] Kim J et al. Stability and convergence of sequential methods for coupled flow and geomechanics: Fixed-stress and fixed-strain splits, Comput. Methods Appl. Mech. Eng. 2011; 200, 1591–1606.

[84] Kim J et al. Stability, accuracy and efficiency of sequential methods for coupled flow and geomechanics, Soc. Pet. Eng. J. 2011, 16(2), 249–262.

[85] Kim J et al. Rigorous coupling of geomechanics and multiphase flow with strong capillarity, Soc. Pet. Eng. J. 2013; 18(6), 1123–1139.

[86] Lackner KS. A guide to CO2 sequestration, Science 2003; 300(5626), 1677–1678.

[87] LaGriT Manual, Los Alamos Natl. Lab., Los Alamos, N. M.; 2013.

[88] Lei XY et al. Application of contact-friction interface element to tunnel excavation in faulted rock, Comput. Geotech. 1995; 17, 349–370.

[89] LeVeque RJ. Finite Volume Methods for Hyperbolic Problems, Cambridge Univ. Press, Cambridge, U. K.; 2002.

[90] Lewis RW, Schrefler BA. The Finite Element Method in the Static and Dynamic Deformation and Consolidation of Porous Media, 2nd ed., John Wiley, Chichester, U. K.; 1998.

[91] Lewis RW, Sukirman Y. Finite element modelling of three-phase flow in deforming saturated oil reservoirs, Int. J. Numer. Anal. Methods Geomech. 1993; 17, 577–598.

[92] Lewis RW et al. Fully coupled modeling of seabed subsidence and reservoir compaction of North Sea oil fields, Hydrogeol. J. 2003; 11(1), 142–161.

[93] Li X et al. Mixed finite element method for coupled thermo-hydro-mechanical process in poro-elastic-plastic media at large strains, Int. J. Numer. Methods Eng. 2005; 64(5), 667–708.

[94] Lofgren BE. Monitoring crustal deformation in The Geyser Clear Lake region, in Research in The Geysers-Clear Lake Geothermal Area, Northern California, p. 1141, U.S. Gov. Print. Off., Washington, D. C.; 1981.

[95] Lomeland F et al. A new versatile relative permeability correlation, paper SCA 2005-32 presented at International Symposium of the Society of Core Analysts, Society of Core Analysts, Toronto, Canada; 2005.

[96] Lomnitz C. Earthquakes and reservoir impounding: State of the art, Eng. Geol. 1974; 8, 191–198.

[97] Mainguy M, Longuemare P. Coupling fluid flow and rock mechanics: Formulations of the partial coupling between reservoir and geomechanics simulators, Oil Gas Sci. Technol. 2002; 57, 355–367.

[97] Mandel J. Consolidation of soils (mathematical study), Geotechnique 1953; 3, 287–299.

[98] Marone C. Laboratory-derived friction laws and their application to seismic faulting, Annu. Rev. Earth Planet. Sci. 1998; 26, 643–696.

[100] McCain WD, Jr. The Properties of Petroleum Fluids, PennWell Books, Tulsa, Okla.; 1990.

[101] Minkoff SE et al. Coupled fluid flow and geomechanical deformation modeling, J. Pet. Sci. Eng. 2003; 38, 37–56.

[102] Molinero J et al. Numerical modeling of the transient hydrogeological response produced by tunnel construction in fractured bedrocks, Eng. Geol. 2002; 64(4), 369–386.

[103] Morris JP et al. The large-scale geomechanical and hydrogeological effects of multiple CO2 injection sites on formation stability, Int. J. Greenh. Gas Control 2011; 5(1), 69–74.

[104] Morris JP et al. A study of injection-induced mechanical deformation at the In Salah CO2 storage project, Int. J. Greenh. Gas Control 2011; 5(2), 270–280.

[105] Mossop A, Segall P. Subsidence at The Geysers geothermal field, N. California from a comparison of GPS and leveling surveys, Geophys. Res. Lett. 1997; 24, 1839–1842.

[106] Muskat M. Physical Principles of Oil Production, McGraw-Hill, New York, N. Y.; 1949.

[107] Nikooee E et al. Effective stress in unsaturated soils: A thermodynamic approach based on the interfacial energy and hydromechanical coupling, Transp. Porous Media 2013; 96, 369–396.

[108] Nuth M, Laloui L. Effective stress concept in unsaturated soils: Clarification and validation of a unified framework, Int. J. Numer. Anal. Methods Geomech. 2008; 32, 771–801.

[109] Okada Y. Internal deformation due to shear and tensile faults in a half-space, Bull. Seismol. Soc. Am. 1992; 82, 1018–1040.

[110] Orr F. M., Jr. Onshore geologic storage of $CO_2$, Science 2009; 325, 1656–1658.

[111] Osborn SG et al. Methane contamination of drinking water accompanying gas-well drilling and hydraulic fracturing, Proc. Natl. Acad. Sci. U. S. A. 2011; 108(20), 8172–8176.

[112] Pacala S, Socolow R. Stability wedges: Solving the climate problem for the next 50 years with current technologies, Science 2004; 305, 968–972.

[113] Pan H, Cao H. User Manual for General Purpose Research Simulator, Stanford Univ. Pet. Eng. Inst., Stanford, Calif.; 2010.

[114] Pao WKS, Lewis RW. Three dimensional finite element simulation of three-phase flow in a deforming fissured reservoir, Comput. Methods Appl. Mech. Eng. 2002; 191, 2631–2659.

[115] Park KC. Stabilization of partitioned solution procedure for pore fluid–soil interaction analysis, Int. J. Numer. Methods Eng. 1983; 19, 1669–1673.

[116] Phillips PJ, Wheeler MF. A coupling of mixed and continuous Galerkin finite element methods for poroelasticity I: The continuous in time case, Comput. Geosci. 2007; 11, 131–144.

[117] Phillips PJ, Wheeler MF. A coupling of mixed and continuous Galerkin finite element methods for poroelasticity II: The discrete-in-time case, Comput. Geosci. 2007; 11, 145–158.

[118] Raleigh CB et al. An experiment in earthquake control at Rangely, Colorado, Science 1976, 191, 1230–1237.

[119] Reasenberg PA, Simpson RW. Response of regional seismicity to the static stress change produced by the Loma Prieta earthquake, Science 1992; 255, 1687–1690.

[120] Rice J. Fault Stress States, Pore Pressure Distributions, and the Weakness of the San Andreas Fault, pp. 475–503, Academic Press, London, U. K.; 1992.

[121] Rice J. Spatio-temporal complexity of slip on a fault, J. Geophys. Res. 1993; 98, 9885–9907.

[122] Roeloffs E. Poroelastic techniques in the study of earthquake-related hydrologic phenomena, Adv. Geophys. 1996; 37, 135–195.

[123] Ruina AL. Slip instability and state variable friction laws, Geophys. Res. Lett. 1983; 88, 359–370.

[124] Rutqvist J et al. A modeling approach for analysis of coupled multiphase fluid flow, heat transfer, and deformation in fractured porous rock, Int. J. Rock Mech. Min. Sci. 2002; 39, 429–442.

[125] Rutqvist J et al. Estimating maximum sustainable injection pressure during geological seques- tration of $CO_2$ using coupled fluid flow and geomechanical fault-slip analysis, Energy Convers. Manage. 2007; 48, 1798–1807.

[126] Rutqvist J et al. Coupled reservoir–geomechanical analysis of the potential for tensile and shear failure associated with $CO_2$ injection in multilayered reservoir–caprock systems, Int. J. Rock Mech. Min. Sci. 2008; 45, 132–143.

[127] Rutqvist J et al. Coupled reservoir-geomechanical analysis of $CO_2$ injection and ground deformations at In Salah, Algeria, Int. J. Greenh. Gas Control 2010; 4, 225–230.

[128] SAMG User's Manual, Fraunhofer Inst. for Algorithms and Sci. Comput. (SCAI), Sankt Augustin, Germany; 2010.

[129] Samier P, Gennaro S. A practical iterative scheme for coupling geomechanics with reservoir simulation, paper SPE 107077 presented at SPE Europec/EAGE 2007, Society of Petroleum Engineers, London, U. K.

[130] Schlumberger Eclipse 100 Reference Manual 2009.1, Schlumberger Inf. Solutions, Houston, Tex.; 2009.

[131] Scholz CH. Mechanics of faulting, Annu. Rev. Earth Planet. Sci. 1989; 17, 309–334.

[132] Segall P. Earthquakes triggered by fluid extraction, Geology 1989; 17, 942–946.

[133] Segura JM, Carol I. On zero-thickness interface elements for diffusion problems, Int. J. Numer. Anal. Methods Geomech. 2004; 28, 947–962.

[134] Segura JM, Carol I. Coupled HM analysis using zero-thickness interface elements with double nodes. Part I: Theoretical model, Int. J. Numer. Anal. Methods Geomech. 2008; 32, 2083–2101.

[135] Segura JM, Carol I. Coupled HM analysis using zero-thickness interface elements with double nodes. Part II: Verification and application, Int. J. Numer. Anal. Methods Geomech. 2008; 32, 2103–2123.

[136] Settari A, Mourits F. A coupled reservoir and geomechanical simulation system, Soc. Pet. Eng. J. 1998; 3, 219–226.

[137] Settari A, Walters DA. Advances in coupled geomechanical and reservoir modeling with applications to reservoir compaction, Soc. Pet. Eng. J. 2001; 6, 334–342.

[138] Sibson RH. Fault rocks and fault mechanisms, J. Geol. Soc. 1977; 133, 191–213.

[139] Sibson RH. Fluid flow accompanying faulting: Field evidence and models, in Earthquake Prediction: An International Review, Maurice Ewing Ser., vol. 4, pp. 593–603, AGU, Washington, D. C.; 1981.

[140] Sibson RH. Brecciation processes in fault zone: Inferences from earthquake rupturing, Pure Appl. Geophys. 1986; 124, 159–175.

[141] Sibson RH. Rupture nucleation on unfavorably oriented faults, Bull. Seismol. Soc. Am. 1990; 80, 1580–1604.

[142] Sibson RH. Crustal stress, faulting and fluid flow, Geol. Soc. Spec. Publ. 1994; 78, 69–84.

[143] Skempton AW. The pore pressure coefficients A and B, Geotechnique 1954; 4, 143–147.

[144] Sukirman Y, Lewis RW. A finite element solution of a fully coupled implicit formulation for reservoir simulation, Int. J. Numer. Anal. Methods Geomech. 1993; 17(10), 677–698.

[145] Szulczewski ML et al. Lifetime of carbon capture and storage as a climate-change mitigation technology, Proc. Natl. Acad. Sci. U. S. A. 2012; 109(14), 5185–5189.

[146] Teatini P et al. Geomechanical response to seasonal gas storage in depleted reservoirs: A case study in the Po River basin, Italy, J. Geophys. Res. 2011; 116, F02002, doi:10.1029/2010JF001793.

[147] Terzaghi K et al. Soil Mechanics in Engineering Practice, John Wiley, New York, N. Y.; 1996.

[148] Thomas LK et al. Coupled geomechanics and reservoir simulation, Soc. Pet. Eng. J. 2003; 8(4), 350–358.

[149] Tran D et al. New iterative coupling between a reservoir simulator and a geomechanics module, Soc. Pet. Eng. J. 2004; 9(3), 362–369.

[150] Tran D et al. Improved iterative coupling of geomechanics with reservoir simulation, paper SPE 93244 presented at SPE Reservoir Simulation Symposium 2005; Society of Petroleum Engineers, Houston, Tex.

[151] van der Elst, NJ et al. Enhanced remote earthquake triggering at fluid-injection sites in the midwestern United States, Science 2013, 341, 164–167.

[152] van Genuchten MT. A closed-form equation for predicting the hydraulic conductivity of unsaturated soils, Soil Sci. Soc. Am. 1980, 44, 892–898.

[153] Vlahinic I et al. A novel and general form of effective stress in a partially saturated porous material: The influence of microstructure, Mech. Mater. 2011; 43, 25–35.

[154] Wan J et al. Stabilized finite element methods for coupled geomechanics-reservoir flow simulations, paper SPE 79694 presented at SPE Reservoir Simulation Symposium 2003; Society of Petroleum Engineers, Houston, Tex.

[155] Wang CY et al. Coseismic hydrologic response of an alluvial fan to the 1999 Chi-Chi earthquake, Taiwan, Geology 2001, 29, 831–834.

[156] Wang HF. Theory of Linear Poroelasticity with Applications to Geomechanics and Hydrogeology, Princeton Univ. Press, Princeton, N. J.; 2000.

[157] Warner NR et al. Geochemical evidence for possible natural migration of Marcellus Formation brine to shallow aquifers in Pennsylvania, Proc. Natl. Acad. Sci. U. S. A. 2012, 109(30), 11,961–11,966.

[158] Warner NR et al. Reply to Engelder: Potential for fluid migration from the Marcellus Formation remains possible, Proc. Natl. Acad. Sci. U. S. A. 2012; 109(52), E3626.

[159] Yerkes RF, Castle RO. Seismicity and faulting attributable to fluid extraction, Eng. Geol. 1976; 10, 151–167.

[160] Zienkiewicz OC, Taylor RL. The Finite Element Method for Solid and Structural Mechanics, Elsevier, Burlington, Mass.; 2005.

[161] Zienkiewicz OC et al. Unconditionally stable staggered solution procedure for soil–pore fluid interaction problems, Int. J. Numer. Methods Eng. 1988; 26(5), 1039–1055.

[162] Zoback MD, Gorelick SM. Earthquake triggering and large-scale geologic storage of carbon dioxide, Proc. Natl. Acad. Sci. U. S. A. 2012, 109, 10,164–10,168.

[163] Zoback MD, Gorelick SM. Reply to Juanes et al.: Evidence that earthquake triggering could render long-term carbon storage unsuccessful in many regions, Proc. Natl. Acad. Sci. U. S. A. 2012; 109(52), E3624.